INORGANIC CHEMISTRY FRONTIERS

RESEARCH ARTICLE

View Article Online
View Journal | View Issue

Cite this: *Inorg. Chem. Front.*, 2025, **12**, 8128

Mn^{2+}-doping and vacancy engineering induce a phase transition with an ultrahigh dielectric switching ratio in lead chloride hybrids

Wei Ye,[a,b] Gang Chen,[a] Dong-Sheng Shao,*[a] Jia-Yi Zhang,[a] Yueqi Shen,[c] Xiao-Zu Wang,[b] Weihua Ning, *[c] Zheng-Fang Tian [d] and Xiao-Ming Ren *[a]

Received 5th September 2025,
Accepted 5th October 2025

DOI: 10.1039/d5qi01839k

rsc.li/frontiers-inorganic

Lead halide hybrids are promising switchable dielectric materials owing to their structural tunability, which enables thermotropic phase transitions. However, achieving large dielectric contrasts remains a significant challenge. Here, we demonstrate a strategy to markedly enhance the dielectric switching ratio (DSR) by engineering a phase-transition compound with elevated ionic conduction in the high-temperature phase *via* vacancy-enabled ionic transport. Using $[C_5H_{12}N]_2PbCl_4$ ($C_5H_{12}N^+$ = piperidinium) as a model, we synthesized a series of $[C_5H_{12}N]_{2-2x}Pb_{1-x}Mn_xCl_{4-2x}$ (x = 0.01–0.15) *via* solvent-free mechanochemistry. Mn^{2+}-doping introduces charge-compensating $C_5H_{12}N^+$ and Cl$^-$ vacancies into the lattice, triggering a structural phase transition. As anticipated, the doped hybrids exhibit a substantially improved DSR, with the x = 0.15 composition reaching an ultrahigh value of ~10^3, surpassing most reported dielectric switching materials. This enhancement is attributed to a grain boundary-induced barrier layer mechanism within the ion-conducting system. Our results establish vacancy-enabled ionic transport as a viable strategy for designing high-performance dielectric switching materials within soft halide frameworks.

Introduction

Switchable dielectric materials exhibit abrupt, reversible changes in dielectric response under external stimuli (temperature, electric field, or pressure), attracting significant interest for tunable capacitors,[1–3] non-volatile memory,[4–6] and smart sensors.[7–9] A key performance metric is the DSR, defined as the permittivity ratio between distinct structural/dynamic states.[10] A high DSR enables both sharp signal contrast and improved energy efficiency in devices.[11,12] Nevertheless, achieving materials that simultaneously deliver a large dielectric contrast, thermal reversibility, and structural stability remains challenging.[13–17]

Lead halide hybrids represent a promising platform for switchable dielectrics.[18–25] Their unique architecture combines rigid inorganic frameworks (1D–3D) with flexible, designable organic cations, enabling thermally driven order–disorder transitions.[26–31] In these phase-transition materials, immobilized dipoles suppress permittivity in the low-temperature phase (LTP), while reorientable cations enhance polarization in the high-temperature phase (HTP). Consequently, rational structural design of organic cations enables precise control over dipole dynamics and phase behavior.

Theoretically, enhancing the DSR in a lead halide hybrid exhibiting a phase transition involves two primary strategies: (i) suppressing permittivity in the LTP by immobilizing dipoles or (ii) boosting permittivity in the HTP by activating additional polarization mechanisms. The latter strategy, boosting HTP permittivity, can be achieved by enhancing ionic conduction. In solid-state ion conductors, elevated permittivity often stems from mechanisms like grain boundary-induced barrier layers.[32–34] Consequently, materials exhibiting thermally switchable ionic conductivity, specifically those acting as ionic insulators in the LTP but becoming ionic conductors in the HTP, represent a promising platform for achieving a high DSR.

To validate this concept, we employed the lead chloride hybrid $[C_5H_{12}N]_2PbCl_4$ ($C_5H_{12}N^+$ = piperidinium) as a model compound. This hybrid undergoes a structural phase transition involving an order–disorder transformation of the organic cations accompanied by distortion of the inorganic framework.[35] Using solvent-free mechanochemical synthesis, we introduced $MnCl_2$ into the host lattice to prepare a series of

---

[a] *State Key Laboratory of Materials-Oriented Chemical Engineering and College of Chemistry and Molecular Engineering, Nanjing Tech University, Nanjing 211816, P. R. China. E-mail: shaods@njtech.edu.cn, xmren@njtech.edu.cn*
[b] *College of Chemistry Engineering, Nanjing Tech University, Nanjing 211816, P. R. China*
[c] *State Key Laboratory of Bioinspired Interfacial Materials Science, Institute of Functional Nano & Soft Materials (FUNSOM), Soochow University, Suzhou, 215123 P. R. China. E-mail: whning@suda.edu.cn*
[d] *Hubei Key Laboratory for Processing and Application of Catalytic Materials, Huanggang Normal University, Huanggang 438000, P. R. China*

$[C_5H_{12}N]_{2-2x}Pb_{1-x}Mn_xCl_{4-2x}$ alloy hybrids (x = 0.01–0.15). Mn^{2+}-doping generated charge-compensating vacancies for both piperidinium cations ($2x$) and Cl^- anions ($2x$), which not only induced a new phase transition but also produced a pronounced ionic conductivity contrast between phases; the hybrids act as ionic insulators in the LTP and as ionic conductors in the HTP. This switchable ion transport mechanism underpins the significantly enhanced DSR.

Results and discussion

Plate-like single crystals of the piperidinium-based hybrid compound $[C_5H_{12}N]_2PbCl_4$ were obtained by crystallization from a saturated DMF solution *via* cooling, and the crystal structure is shown in Fig. 1a.[36] The experimental powder X-ray diffraction (PXRD) pattern matches well with the simulated one, and Pawley refinement of the experimental PXRD pattern yielded unit cell parameters of a = 22.494(8) Å, b = 23.863(10) Å, c = 6.180(2) Å, and V = 3317.3(2) Å^3, consistent with the single-crystal analysis data. Pawley refinement also yielded reasonable R_p and R_{wp} values, confirming the formation of a crystalline sample of $[C_5H_{12}N]_2PbCl_4$ with high phase purity (Fig. S1).

The Mn^{2+}-doped alloy hybrids $[C_5H_{12}N]_{2-2x}Pb_{1-x}Mn_xCl_{4-2x}$ were prepared using a mechanical ball-milling approach, with the molar fraction of Mn x = 0.01, 0.05, 0.10, and 0.15. Notably, alloy hybrids with $x > 0.15$ exhibit poor stability due to moisture absorption in air. This instability is attributed to the preference of Mn^{2+} (a Lewis hard acid) to bind with water in air rather than Cl^- (a Lewis soft base). Therefore, we focused our investigation on alloy hybrids with compositions x = 0.01–0.15. The relative contents of Pb and Mn in the alloys, determined using the inductively coupled plasma (ICP) technique, confirmed that the resulting Mn/Pb molar ratios in each alloy hybrid closely agree with the feed ratios (Table S1). Field-emission scanning electron microscopy (FESEM, Fig. S2 and S3) revealed that the alloy hybrids consist of well-faceted, slightly rounded tetragonal grains with sizes of ≈1 µm. Energy-dispersive X-ray spectroscopy (EDS) elemental mapping (Fig. S2 and S3) showed a homogeneous distribution of C, N, Pb, Mn, and Cl throughout the particle surfaces for each alloy hybrid.

PXRD patterns of the alloy hybrids obtained using gold foil as an internal reference (2θ = 37.88° and 44.08°)[37] are displayed in Fig. 1b. These patterns are highly similar to that of the parent compound $[C_5H_{12}N]_2PbCl_4$, demonstrating that Mn^{2+} doping does not destroy the parent crystal structure. Pawley refinement of the alloy PXRD patterns (Fig. S4) indicated no secondary phases. Notably, doping Mn^{2+} ions and vacancies into the $[C_5H_{12}N]_2PbCl_4$ lattice results in non-monotonic variation of the crystallographic plane distances. As shown in Fig. 1c, the diffraction peak position of the (020) crystallographic plane remains unchanged for the x = 0.01 alloy, while it shifts to a higher diffraction angle for the x = 0.05 alloy. With further increases in Mn^{2+} content (x = 0.10 and 0.15), the (020) diffraction peak shifts back toward lower angles and develops a shoulder on the lower-angle side (Fig. 1d). Pawley refinements further demonstrated an initial contraction followed by an expansion of the unit cell parameters (a, b, c, and V) as Mn content increases (Fig. 1e). These results indicate that at low doping levels, Mn^{2+} primarily substitutes for Pb^{2+} within the $[PbCl_4{}^{2-}]_\infty$ chains, reducing the interplanar spacing due to its smaller ionic radius (Mn^{2+} = 0.87 Å *vs.* Pb^{2+} = 1.33 Å).[38,39]

To investigate the thermal stability of all alloy hybrids, thermogravimetric analysis (TGA) was performed from 303 to

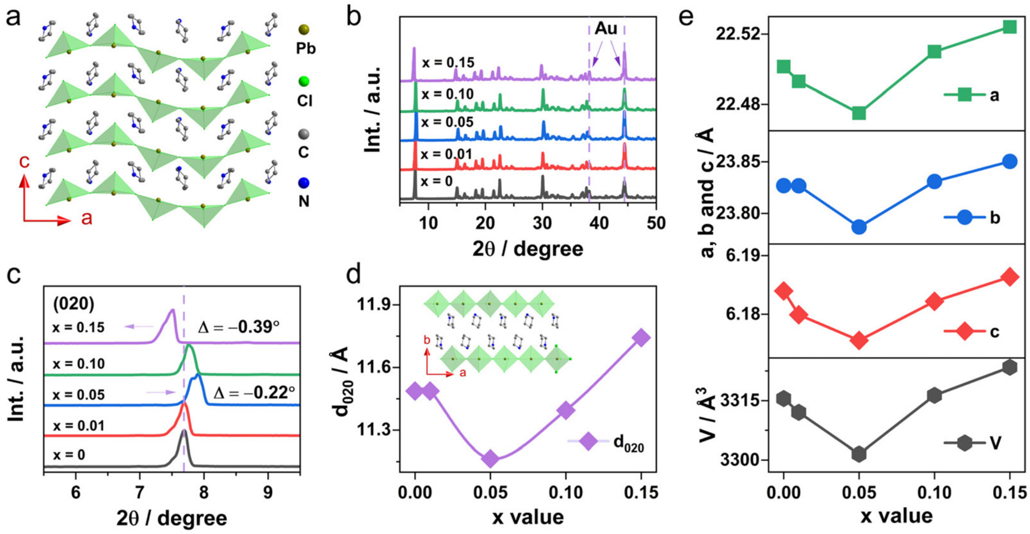

Fig. 1 $[C_5H_{12}N]_{2-2x}Pb_{1-x}Mn_xCl_{4-2x}$: (a) crystal structure of x = 0, (b) PXRD patterns of x = 0–0.15, (c) magnified view of the (020) diffraction peak of x = 0–0.15, (d) d_{020} change with x for x = 0–0.15, and (e) refined unit cell parameters obtained using PXRD patterns in the 2θ range of 5–120° for x = 0–0.15.

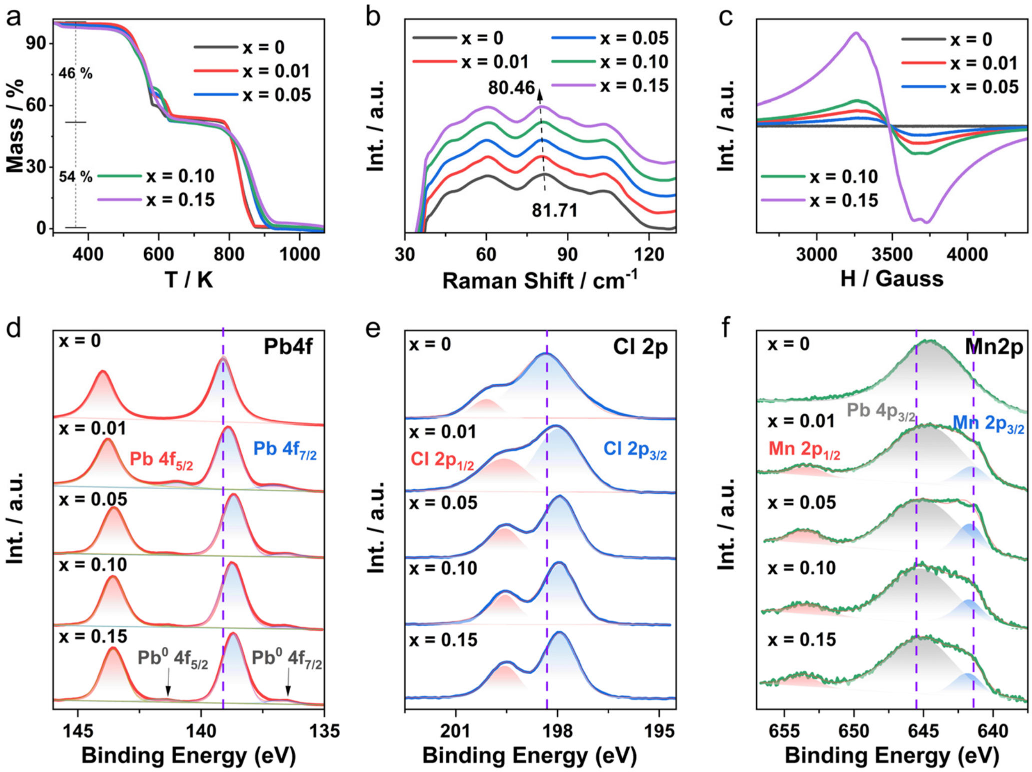

Fig. 2 $[C_5H_{12}N]_{2-2x}Pb_{1-x}Mn_xCl_{4-2x}$: (a) TG plots of x = 0–0.15 under an N_2 atmosphere in the 300–1000 K range, (b) Raman spectra of x = 0–0.15 at ambient temperature in the 30–130 cm^{-1} range, (c) EPR spectra of x = 0.01–0.15 at ambient temperature, and (d–f) XPS spectra of Pb $4f_{5/2}$, Pb $4f_{7/2}$, Cl $2p_{1/2}$, Cl $2p_{3/2}$, Mn $2p_{1/2}$ and Mn $2p_{3/2}$ for x = 0–0.15.

1073 K (Fig. 2a). The resulting TG plots are highly analogous, exhibiting three distinct weight-loss processes. The first process (<373 K) corresponds to the loss of adsorbed surface or lattice-vacancy water. The second process (>460 K) involves decomposition of the $[C_5H_{12}N]Cl$ component,[40] leaving $MnCl_2$/$PbCl_2$ as the primary residue. Upon further heating (≈770 K), this residue melts and partially volatilizes. Notably, the onset decomposition temperature of the $[C_5H_{12}N]Cl$ component increases slightly with higher Mn content (x = 0.05–0.15). This shift is attributed to the greater thermal stability of $MnCl_2$ relative to $PbCl_2$.[41,42]

Raman and IR spectra of $[C_5H_{12}N]_{2-2x}Pb_{1-x}Mn_xCl_{4-2x}$ (x = 0–0.15) are shown in Fig. 2b and Fig. S5 and S6 with detailed vibrational assignments in Tables S2 and S3. The Raman spectra exhibit multiple bands between 34 and 130 cm^{-1} (Fig. 2b). For the parent compound ($[C_5H_{12}N]_2PbCl_4$), the bands at 46, 60, and 80 cm^{-1} are assigned to Pb–Cl scissoring modes, while the band at 104 cm^{-1} corresponds to a Pb–Cl stretching mode.[43,44] In the alloy hybrids, the Pb–Cl scissoring bands red-shift with increasing x, reaching a shift of ≈1.25 cm^{-1} for x = 0.15. This indicates local chemical environments altered due to Mn^{2+} substitution. The Raman and IR spectra are nearly identical in the 500–3200 cm^{-1} region (Fig. S6) across all compositions (x = 0–0.15). Since bands in this region originate from organic cation vibrations, this consistency demonstrates that Mn^{2+} doping induces small perturbation to the organic moieties. Consequently, Mn^{2+} incorporation is confined to the inorganic framework.

Electron paramagnetic resonance (EPR) spectra were collected at room temperature (Fig. 2c and Fig. S7). Pristine $[C_5H_{12}N]_2PbCl_4$ (x = 0) exhibited EPR silence, while alloy hybrids (x = 0.01–0.15) display a broad isotropic signal characteristic of Mn^{2+} ions, with a g-factor of approximately 2.0 for each alloy hybrid (Table S4).[45,46] Although hyperfine features arising from electron–nuclear spin interactions are present, fully resolved sextet signals are not observed. This broadening is likely due to strong dipole–dipole coupling between neighboring Mn^{2+} ions. The broad, isotropic signal lacking a clear hyperfine structure alongside strong dipole–dipole coupling between Mn^{2+} ions suggests that Mn^{2+} occupies symmetric lattice sites and may form magnetic clusters within the host lattice.

High-resolution X-ray photoelectron spectroscopy (XPS) core-level spectra of C 1s, N 1s, Pb 4f, Mn 2p, and Cl 2p are shown in Fig. 2d–f and Fig. S8–10, with binding energies summarized in Table S5. For the x = 0 hybrid, the Pb $4f_{7/2}$ and $4f_{5/2}$ peaks at 139.07 eV and 143.99 eV correspond to Pb^{2+}. These peaks systematically shift towards lower binding energies with increasing x, reaching a total shift of 0.44 eV for x = 0.15. A weak component at 136.98 eV/140.94 eV is assigned to metallic Pb^0, associated with halide deficiency and unsaturated Pb sites.[47] The Cl $2p_{3/2}$ and $2p_{1/2}$ peaks for x = 0 (located at 201.68

and 199.88 eV, consistent with Cl^- literature values[48,49]) also shift to lower binding energies compared to those of the pristine sample (Fig. 2f). For $x = 0.01$, the Mn $2p_{3/2}$ and $2p_{1/2}$ peaks appear at 641.98 eV and 653.78 eV, respectively. With increasing Mn content, these peaks shift towards higher binding energies. The binding energies of C 1s and N 1s also increase with higher Mn content (Table S5). The systematic binding energy shifts demonstrate that Mn^{2+} doping modifies the electronic structure; *i.e.*, decreasing Pb^{2+} and Cl^- binding energies suggest an increase in electron density around these ions. Increasing Mn^{2+} binding energies indicate a decrease in electron density around the Mn ions. These XPS results confirm the successful incorporation of Mn^{2+} into the lead chloride hybrid lattice and reveal significant doping-induced modifications in the electronic structure and local chemical environment of all components.

Differential scanning calorimetry (DSC) measurements for compositions $x = 0$–0.15 (273–453 K) are presented in Fig. 3a and Fig. S11. The pristine compound ($x = 0$) exhibits a reversible thermal anomaly at 355.5 K (heating) and 342.7 K (cooling), corresponding to a known phase transition. This reversible anomaly persists in all vacancy-doped alloy hybrids ($x = 0.01$–0.15). Significantly, all alloy hybrids display an additional, distinct thermal anomaly at higher temperatures (≈410–420 K during heating; Fig. 3a and Fig. S11). For clarity, phases are denoted sequentially from low to high temperature as phase I to phase IV. However, because the temperature interval between phase III and phase IV is narrow (<20 K) upon heating, and because these two phases merge during cooling, they are collectively designated as phase III. Notably, these emergent anomalies are fully reproducible over successive heating–cooling cycles, and their critical temperatures are independent of the thermal history. We attribute these additional thermal events to the introduction of Mn^{2+} ions and vacancies.

As shown in Fig. 3a, increasing the doping concentration (x) induces two key trends: (1) the peak temperature of the low-temperature anomaly shifts slightly downward, while (2) the peak temperature of the doping-induced high-temperature anomaly shifts slightly upward. We calculated the enthalpy (ΔH) and entropy (ΔS) changes for each phase transition in the $[C_5H_{12}N]_{2-2x}Pb_{1-x}Mn_xCl_{4-2x}$ with $x = 0$–0.15. As summar-

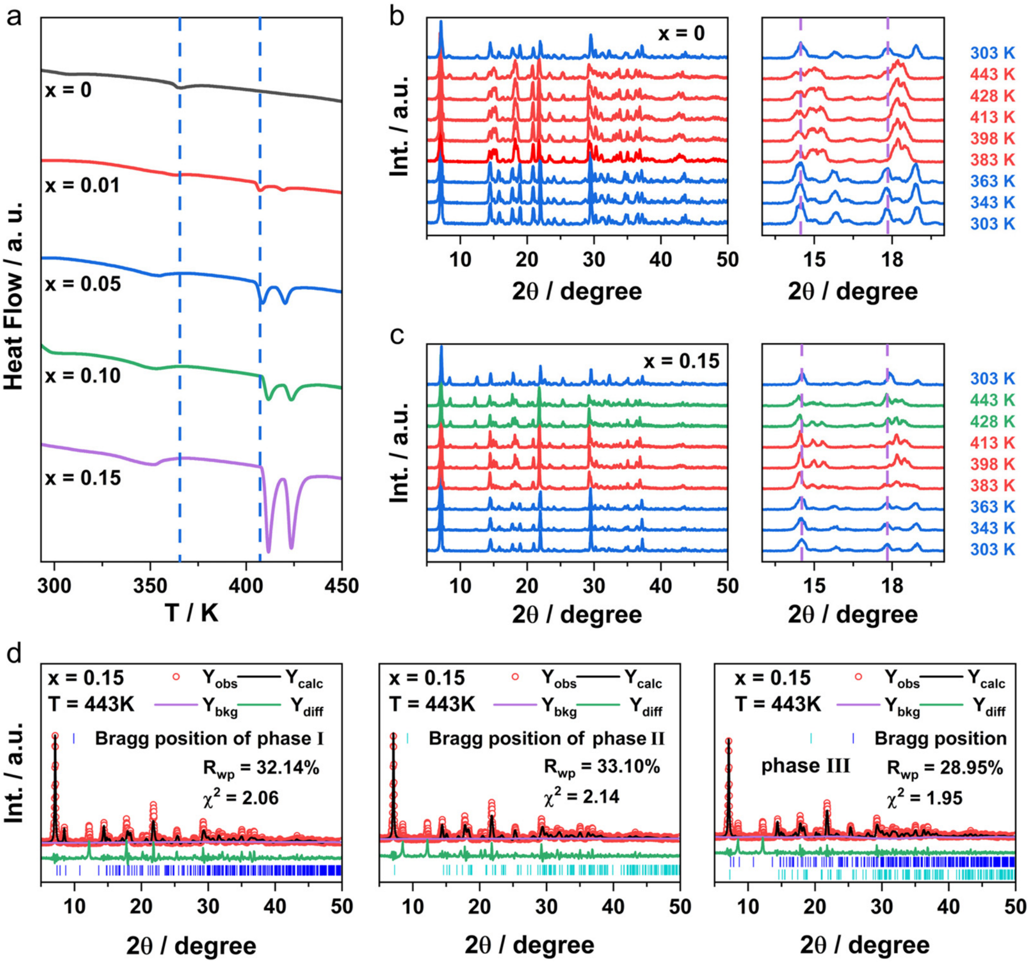

Fig. 3 $[C_5H_{12}N]_{2-2x}Pb_{1-x}Mn_xCl_{4-2x}$: DSC plots of $x = 0$–0.15 (a) and variable-temperature PXRD patterns of $x = 0$ (b) and 0.15 (c). Rietveld refinement of the PXRD patterns of $x = 0.15$ in the 2θ range of 5–50° based on phase I, phase II, and phase I + II models (d).

Table 1 The onset/peak temperature (T_{onset}/T_{peak}, K), change of enthalpy (ΔH, J mol^{-1}) and entropy (ΔS, J mol^{-1} K^{-1}) of the phase transition

		Transition between phases I and II			Transition between phases II and III		
Sample	Process	T_{onset}/T_{peak}	ΔH	ΔS	T_{onset}/T_{peak}	ΔH	ΔS
$x = 0$	Heating	360.5/365.3	320.9	0.9	—	—	—
	Cooling	357.9/349.1	246.8	0.7	—	—	—
$x = 0.01$	Heating	347.9/363.3	364.6	1.0	404.4/407.2 and 412.9/419.5	229.1/167.9	0.6/0.4
	Cooling	357.1/347.6	575.8	1.7	388.8/384.9	206.4	0.5
$x = 0.05$	Heating	333.7/353.6	514.9	1.5	405.3/408.5 and 415.0/420.4	600.6/553.7	1.5/1.3
	Cooling	349.2/337.2	677.1	2.0	395.8/389.3	867.9	2.2
$x = 0.10$	Heating	331.2/352.7	728.1	2.1	407.9/411.7 and 418.9/423.5	619.2/651.6	1.5/1.5
	Cooling	342.2/328.0	702.8	2.1	396.8/391.6	1018.7	2.6
$x = 0.15$	Heating	322.8/352.7	1107.1	3.1	408.4/411.5 and 419.8/423.6	1950.1/2216.7	4.7/5.2
	Cooling	340.6/321.9	851.7	2.65	401.5/397.8	3688.9	9.3

ized in Table 1 and Fig. S12, both ΔH and ΔS values increase systematically with higher doping concentrations (x). Since ΔS is related to the degree of disorder of a system, an increase in ΔS during phase transitions signifies greater system disorder. This demonstrates that lattice disorder increases with increasing x in the alloy hybrids.

All hybrids exhibit similar PXRD patterns in phase I and phase II (Fig. 1a, 3b, and 3c and Fig. S1, S4, and S13), respectively. This similarity implies that the phase I ↔ phase II transition shares an analogous origin across the alloy series. Single-crystal structure analysis of $[C_5H_{12}N]_2PbCl_4$ reveals that its thermal anomaly corresponds to a structural phase transition.[35] This parent compound crystallizes in the orthorhombic space group *Pnma* in phase I and the monoclinic space group *C*2/*c* in phase II (Fig. S14). Notably, the high-temperature phase II exhibits lower symmetry than the low-temperature phase I, contrasting the typical 'symmetry-breaking' phase transition observed in most materials. This unusual behavior classifies the transition as an inverse symmetry-breaking process, driven by order–disorder transformations of piperidinium cations and structural reorganization of the anionic framework from one-dimensional vertex-sharing square-pyramidal chains to two-dimensional vertex-sharing octahedral layers.[35] Consequently, the phase I ↔ phase II transition in all alloy hybrids is driven by analogous order–disorder transformations of cations and structural reorganization of the anionic framework. Increasing x elevates the concentration of cationic vacancies and Cl^- vacancies, and this increases the cation free volume, promoting the order–disorder transformation of cations at lower temperatures, consistent with DSC observations.

For the alloy hybrids, the transition from phase II to phase III preserves most diffraction peaks from phase II while introducing several new peaks. Significantly, these new peaks closely resemble those characteristic of phase I. For instance, a peak at $2\theta = 17.8°$ appears in the PXRD pattern of the $x = 0.15$ alloy hybrid at 443 K. This suggests that phase III may be a mixture containing domains isomorphic to phase I and phase II, respectively.

To verify this, we conducted Rietveld refinement of the PXRD pattern for the $x = 0.15$ alloy hybrid at 443 K, evaluating models based on phase I alone, phase II alone, and a combination of both phases. As shown in Fig. 3d, the mixed-phase model provided a reasonable fit, yielding a phase II to phase I content ratio of approximately 0.7 : 0.3. This indicates that upon heating above the phase II to phase III transition temperature, a portion of phase II transforms back into phase I. This re-entrant phase behavior (reappearance of a lower-temperature phase upon heating) can be understood thermodynamically, *i.e.*, the thermally activated dynamics of the cations increase their disorder. This heightened disorder promotes a lattice transformation from the lower-symmetry phase II back to the higher-symmetry phase I structure.

The combination of high-resolution Rietveld refinements, variable-temperature PXRD, and DSC measurements demonstrates that Mn doping induces a re-entrant order–disorder transition. The parent-like phase I ↔ phase II transformation is retained, while an additional high-temperature mixed-phase state appears, consistent with cation disorder and vacancy-driven lattice reorganization.

The dielectric spectra of $[C_5H_{12}N]_{2-2x}Pb_{1-x}Mn_xCl_{4-2x}$ (x = 0–0.15) were collected from 273 K to 453 K and 1 kHz to 10 MHz. Plots of the real part of the dielectric permittivity (ε') *versus* temperature (T) at selected AC frequencies are shown in Fig. 4a and 4b and Fig. S15 for each compound. For the x = 0 hybrid compound (prepared mechanochemically), ε' ranges from 13.5 to 16.5 between 273 K and 350 K, showing near frequency independence (Fig. 4a). A dielectric anomaly emerges near 350 K upon heating. Above 350 K, the system exhibits thermally activated dielectric relaxation, and the dielectric features are in agreement with the observation in the literature.[35,50–52]

For x = 0.01–0.15 alloy hybrids, ε'–T plots exhibit two key characteristics: (i) between 273 K and 373 K, ε' is nearly frequency independent for all alloy hybrids. However, ε' at fixed temperature and frequency increases with rising x. For example, ε' ranges from 13.5 to 17.4 for $x = 0$, but from 14.3 to 24.8 for $x = 0.15$. (ii) Two dielectric anomalies occur between 273 K and 453 K across all frequencies. The lower-temperature anomaly (≈350 K) shows an unobvious peak shift with x and originates from an inverse broken-symmetry phase transition. The higher-temperature anomaly (≈410 K) also shows a negligible peak shift with x. This transition, induced by Mn^{2+} doping and vacancies, is associated with a structural phase transition.

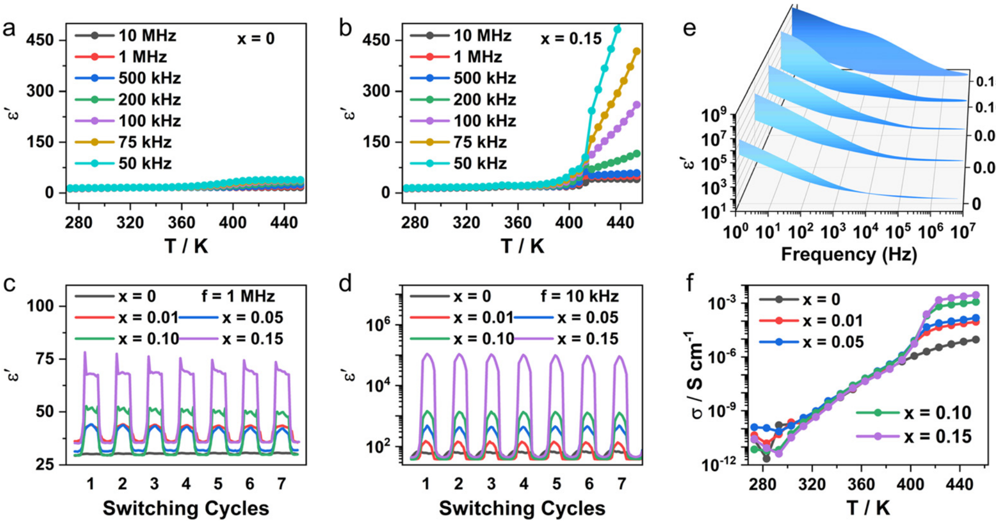

Fig. 4 $[C_5H_{12}N]_{2-2x}Pb_{1-x}Mn_xCl_{4-2x}$: plots of ε' *vs.* T at selected AC frequencies for x = 0 (a) and x = 0.15 (b). Dielectric switching responses for x = 0–0.15 at AC frequencies of 1 MHz (c) and 10 kHz (d). Frequency dependence of the DSR in the 383–433 K range for x = 0–0.15 (e). Plots of σ *vs.* T for x = 0–0.15 (f).

Notably, above ≈410 K, ε' increases abruptly for all alloy hybrids, showing the dielectric characteristics of high-κ materials, and intensifies with increasing x (Fig. S16). This sharp increase results in a switchable dielectric response across this phase transition. Furthermore, thermal cycling demonstrates repeatable switching between a low-ε' state (the 'off' state) and a high-ε' state (the 'on' state). As illustrated in Fig. 4c–e, the dielectric switching behavior was characterized over 383–433 K for seven thermal cycles at 1 MHz and 10 kHz across all alloy compositions. At 10 kHz, the DSR (high ε'/low ε') reaches 2.0, 2.6, 12.3 and 2200 for x = 0.01, 0.05, 0.10, and 0.15, respectively. Remarkably, these switching ratios exceed most reported values for both organic and inorganic perovskite dielectric switching materials (Table S6).

To investigate the origin of high ε', variable-temperature impedance spectra were analyzed for all hybrids (Fig. S17–S21). For x = 0.01–0.15 hybrids, Nyquist plots (Z' *vs.* Z'') below 313 K exhibit near-linear behavior, indicating negligible conduction. Above 313 K, two distinct arcs emerge, corresponding to bulk and grain boundary resistances. Conductivity (σ) was extracted by fitting impedance spectra using ZView software with equivalent circuits (Fig. S22), calculated as:

$$\sigma = \frac{L}{SR} \tag{1}$$

where L is the pellet thickness, S is the electrode contact area, and R is the bulk resistance.

Temperature-dependent conductivity (Fig. 4f) shows that all hybrids exhibit low conduction ($\sigma \approx 10^{-10}$–10^{-7} S cm^{-1}) below 393 K. Crucially, no anomaly appears near the ≈350 K phase transition in σ *vs.* T plots, contrasting sharply with ε' and DSC results, confirming that this dielectric anomaly is not conduction related. However, a sharp conductivity jump occurs near 403 K for all doped hybrids, with the jump magnitude increasing with x. For instance, the σ value of the x = 0.15 alloy hybrid increases gradually from 1.4×10^{-10} S cm^{-1} at 318 K to 1.1×10^{-6} S cm^{-1} at 393 K, followed by a three-order-of-magnitude jump to 1.5×10^{-3} S cm^{-1} at 423 K. It further rises to 2.8×10^{-3} S cm^{-1} at 453 K, indicating significantly enhanced conduction above the doping-induced phase transition temperature.

To distinguish ionic *vs.* electronic conducting contributions, chronoamperometry measurements (313–453 K) were performed (Fig. S23). The change of current with time for the x = 0.15 alloy hybrid shows that the initial exponential decay from ≈22.2 μA to 6.8 μA in ≈2.7 s stems from ionic polarization/transport, and the subsequent steady-state current corresponds to electronic conduction. The extracted electronic conductivity is 8.3×10^{-4} S cm^{-1} at 453 K, ~1 order below its total conductivity from impedance measurements, confirming that ionic transport dominates in all doped hybrids. This dominance of ionic conduction is consistent with the doping mechanism: introducing $MnCl_2$ into the $[C_5H_{12}N]_2PbCl_4$ lattice creates vacancies for both $[C_5H_{12}N]^+$ cations and Cl^- anions. Specifically, in the $[C_5H_{12}N]_{2-2x}Pb_{1-x}Mn_xCl_{4-2x}$ alloy hybrids, this results in $2x$ cation vacancies and $2x$ Cl^- vacancies. These vacancies facilitate cation migration, enabling high ionic conductivity. Consequently, this ionic conduction induces a high-κ response, primarily through the mechanism of grain boundary-induced barrier layers,[26–28] ultimately yielding ultrahigh DSR.

Experimental section

Reagents and materials

Lead(II) chloride ($PbCl_2$, 99.98%), piperidine hydrochloride ($C_5H_{11}N{\cdot}HCl$, 98%), manganese(II) chloride tetrahydrate ($MnCl_2{\cdot}4H_2O$, 99%), and all other reagents were purchased from Macklin and used without further purification.

Synthesis of $[C_5H_{12}N]_2PbCl_4$ crystals

A mixture was prepared by dissolving piperidine hydrochloride (0.08 mol) and $PbCl_2$ (0.04 mol) in *N*,*N*-dimethylformamide (300 mL), followed by heating to 150 °C until a clear precursor solution was obtained. This solution was naturally cooled to ambient temperature. After 48 h, transparent plate-like crystals (yield ≈ 62.3%) formed and were collected by filtration, washed with acetonitrile (3 × 10 mL), and dried in air for subsequent use.

Preparation of $[C_5H_{12}N]_{2-2x}Pb_{1-x}Mn_xCl_{4-2x}$ (x = 0.01, 0.05, 0.10 and 0.14)

A series of Mn-doped alloy hybrids $[C_5H_{12}N]_{2-2x}Pb_{1-x}Mn_xCl_{4-2x}$ were prepared using a mechanical ball milling method. Specifically, $[C_5H_{12}N]_2PbCl_4$ and $MnCl_2$ were mixed at an in-feed molar ratio of $(1 - x)/x$ (x = 0.01, 0.05, 0.10 and 0.15), where x is the molar fraction. The resulting mixture was milled in a vibration ball-milling machine (GT300, Beijing Grinder Instrument Co., Ltd., China) with a frequency of 30 Hz for 2 h and then annealed under vacuum at 110 °C for 2 h. The actual Mn^{2+} contents were confirmed by inductively coupled plasma (ICP) analysis (Table S1).

Chemical and physical characterization

Inductively coupled plasma mass spectrometry (ICP-MS) analysis was performed using an Optima 8000. Energy-dispersive X-ray spectroscopy (EDS) elemental mapping was performed using a scanning electron microscope (Quanta FEG 250, Elect Plus). Powder X-ray diffraction (PXRD) data at ambient temperature were collected using a MiniFlex600 powder diffractometer equipped with a Cu K_α radiation source (λ = 1.54056) and a step size of 0.02° in 2θ angles at ambient temperature, with gold foil as an internal reference. Variable-temperature powder X-ray diffraction (PXRD) measurements were performed using a Rigaku D/MAX 2000 PC X-ray diffractometer in the 2θ range of 5–50° with a step size of 0.02° at selected temperatures. Thermogravimetric (TG) measurements were carried out using a Shimadzu DTG-60H thermogravimetric analyzer under a nitrogen atmosphere at a heating rate of 10 K min^{-1} from room temperature to 1073 K. Differential scanning calorimetry (DSC) measurements were conducted using a Discovery DSC-25 at a temperature change rate of 20 K min^{-1}.

Fourier transform infrared (FT-IR) spectra were recorded using an FT 9700 spectrophotometer within the range of 4000–400 cm^{-1}. Raman spectra were recorded in the spectral range of 3300–23 cm^{-1} using a 785 nm laser source (Thermo Fisher Scientific DXR2). X-ray photoelectron spectroscopy (XPS) was conducted using a Thermo Fisher Nexsa instrument equipped with a standard monochromatic Al K_α X-ray source (72 W, 12 kV, 6 mA), with binding energies referenced to the internal standard C 1s peak at 284.8 eV. X-band electron paramagnetic resonance (EPR) spectra were obtained under ambient conditions using an A200-6/1 EPR spectrometer.

Temperature- and frequency-dependent dielectric spectra for the polycrystal alloy hybrids $[C_5H_{12}N]_{2-2x}Pb_{1-x}Mn_xCl_{4-2x}$ (x = 0.01, 0.05, 0.10 and 0.14) were collected using a concept 80 system (Novocontrol, Germany) in the temperature range of 273–453 K at a heating/cooling rate of 3 K min^{-1} with a holding period at each set point. The powder sample was prepared in the form of a pellet with a 7 mm diameter and 1.4 mm thickness. Both faces of the pellet were coated with conductive silver paste and sandwiched between two parallel Pt electrodes and the AC frequencies span from 1 Hz to 10^7 Hz.

Conclusions

In this study, we present a vacancy-doping strategy to enhance the DSR of dielectric switching materials. Introducing vacancies into the host lattice promotes a high dielectric constant (κ), thereby achieving ultrahigh DSR values. As a proof of concept, we employed a lead chloride hybrid as a model system. By incorporating vacancies into its lattice, we synthesized a series of $[C_5H_{12}N]_{2-2x}Pb_{1-x}Mn_xCl_{4-2x}$ alloy hybrids (x = 0.01–0.15) containing $2x$ cation vacancies and $2x$ Cl^- vacancies. These vacancy-doped hybrids exhibit markedly improved DSR, with the x = 0.15 composition reaching $\approx 10^3$. Our findings demonstrate that vacancy doping is an effective approach for developing dielectric switching materials with large dielectric contrasts.

Author contributions

D. S. Shao, W. Ning and X. M. Ren conceived the idea for the manuscript and designed the experiments; W. Ye, G. Chen, J. Y. Zhang and Y. Shen developed the synthesis procedures and performed the basic chemical and physical characterization; X. Z. Wang and Z. F. Tian assisted with the data analysis; X. M. Ren, W. Ning and D. S. Shao guided the experiments, discussed the data, and led the project; W. Ye wrote the original draft; X. M. Ren, W. Ning and D. S. Shao reviewed and edited the draft with contributions from all authors.

Conflicts of interest

The authors declare no conflict of interest.

Data availability

All data supporting the findings of this study are available in the supplementary information (SI) of this article. Details of PXRD patterns, FESEM images and EDS mapping, FT-IR, EPR, XPS, DSC, Rietveld refinement of the PXRD patterns, temperature-dependent dielectric permittivity and impedance spectra etc. are included in the SI. See DOI: **https://doi.org/10.1039/d5qi01839k**.

Acknowledgements

This work was financially supported by the Priority Academic Program Development of Jiangsu Higher Education

Institutions, the National Nature Science Foundation of China (grant no. 22073047), the Collaborative Innovation Center of Suzhou Nano Science & Technology, the 111 Project, the Joint International Research Laboratory of Carbon-Based Functional Materials and Devices, the Suzhou Key Laboratory of Advanced Photonic Materials (Grant SZS2023010), and the Gusu Innovation and Entrepreneurship Leading Talent Program (ZXL2023188).

References

1 V. Jurečič, T. Rojac, V. Bobnar and N. Novak, Origin of enhanced dielectric tunability in antiferroelectric ceramic systems, *Adv. Funct. Mater.*, 2025, **35**, 2412739.

2 W. Zhang, H. Y. Ye, R. Graf, H. W. Spiess, Y. F. Yao, R. Q. Zhu and R. G. Xiong, Tunable and switchable dielectric constant in an amphidynamic crystal, *J. Am. Chem. Soc.*, 2013, **135**, 5230–5233.

3 A. Ahmed, I. A. Goldthorpe and A. K. Khandani, Electrically tunable materials for microwave applications, *Appl. Phys. Rev.*, 2015, **2**, 011302.

4 H. Yang, S. O. Valenzuela, M. Chshiev, S. Couet, B. Dieny, B. Dlubak, A. Fert, K. Garello, M. Jamet, D. E. Jeong, K. Lee, T. Lee, M. B. Martin, G. S. Kar, P. Sénéor, H. J. Shin and S. Roche, Two-dimensional materials prospects for non-volatile spintronic memories, *Nature*, 2022, **606**, 663–673.

5 D. Kim, S. J. Yang, N. Wainstein, S. Skrzypczak, G. Ducournau, E. Pallecchi, H. Happy, E. Yalon, M. Kim and D. Akinwande, Emerging memory electronics for non-volatile radiofrequency switching technologies, *Nat. Rev. Electr. Eng.*, 2024, **1**, 10–23.

6 S. T. Han, Y. Zhou and V. A. L. Roy, Towards the development of flexible non–volatile memories, *Adv. Mater.*, 2013, **25**, 5425–5449.

7 Z. Wang, M. Rao, R. Midya, S. Joshi, H. Jiang, P. Lin, W. Song, S. Asapu, Y. Zhuo, C. Li, H. Wu, Q. Xia and J. J. Yang, Threshold switching of Ag or Cu in dielectrics: materials, mechanism, and applications, *Adv. Funct. Mater.*, 2018, **28**, 1704862.

8 M. Hussain, H. Zahra, S. M. Abbas and Y. Zhu, Flexible dielectric materials: potential and applications in antennas and RF sensors, *Adv. Electron. Mater.*, 2024, **10**, 2400240.

9 B. Stadlober, M. Zirkl and M. Irimia-Vladu, Route towards sustainable smart sensors: ferroelectric polyvinylidene fluoride-based materials and their integration in flexible electronics, *Chem. Soc. Rev.*, 2019, **48**, 1787–1825.

10 Y. Liu, S. Han, J. Wang, Y. Ma, W. Guo, X. Y. Huang, J. H. Luo, M. Hong and Z. Sun, Spacer cation alloying of a homoconformational carboxylate trans isomer to boost in-plane ferroelectricity in a 2D hybrid perovskite, *J. Am. Chem. Soc.*, 2021, **143**, 2130–2137.

11 H. Nishikawa, K. Sano and F. Araoka, Anisotropic fluid with phototunable dielectric permittivity, *Nat. Commun.*, 2022, **13**, 1142.

12 H. Wang, H. Jiang, Y. Li and C. Zhang, Electric–thermal dual–responsive HASEL actuator for solid–liquid Bi–stabilized smart switching, *Adv. Funct. Mater.*, 2024, **34**, 2409472.

13 J. Harada, M. Takehisa, Y. Kawamura, H. Hasegawa and T. Usui, Solid solutions of plastic/ferroelectric crystals: toward tailor-made functional materials, *J. Am. Chem. Soc.*, 2024, **146**, 21176–21185.

14 J. Harada, T. Shimojo, H. Oyamaguchi, H. Hasegawa, Y. Takahashi, K. Satomi, Y. Suzuki, J. Kawamata and T. Inabe, Directionally tunable and mechanically deformable ferroelectric crystals from rotating polar globular ionic molecules, *Nat. Chem.*, 2016, **8**, 946–952.

15 D. S. Shao, L. Sang, Y. R. Kong, Z. R. Deng, H. B. Luo, Z. F. Tian and X. M. Ren, Tunable thermotropic phase transition triggering large dielectric response and superionic conduction in lead halide perovskites, *Inorg. Chem. Front.*, 2022, **9**, 5653–5662.

16 Y. Gong, J. Zhao, Z. Li, J. Huang, Y. Zhang, L. Dong, C. Xiong and M. Jiang, Unparalleled dielectric–switching effects caused by dual polarization synergy, *Adv. Funct. Mater.*, 2023, **33**, 2214544.

17 Y. Gong, Z. Li, H. Li, W. Wu, W. Zhou, J. Zhao, C. He and M. Jiang, Ultra–tough room–temperature dielectric switching ionic gels with long–cycle Stability, *Adv. Funct. Mater.*, 2022, **32**, 2207452.

18 W. Zhang and R. G. Xiong, Ferroelectric metal–organic frameworks, *Chem. Rev.*, 2012, **112**, 1163–1195.

19 K. Z. Kamali, L. Xu, J. Ward, K. Wang, G. Li, A. E. Miroshnichenko, D. Neshev and M. Rahmani, Reversible image contrast manipulation with thermally tunable dielectric metasurfaces, *Small*, 2019, **15**, 1805142.

20 C. Xue, M. Fujibayashi, H. Huang, C. Kato, K. Ichihashi, J. Manabe, S. Nishihara, X. M. Ren and T. Nakamura, Enhanced electromechanical response in 1D hybrid perovskites: coexistence of normal and relaxor ferroelectric phases, *Adv. Funct. Mater.*, 2025, 2501299.

21 X. Q. Huang, H. Yu, Z. K. Xu, T. Gan and Z. X. Wang, Tuning dielectric transitions in two-dimensional organic–inorganic hybrid lead halide perovskites, *Inorg. Chem.*, 2021, **60**, 16871–16877.

22 J. Li, Z. X. Zhang, T. Zhang, P. Z. Huang, T. Shao, Y. Zhang and D. W. Fu, Switchable dielectric two-dimensional lead-free perovskite with reversible thermochromic response, *J. Phys. Chem. C*, 2022, **126**, 16437–16446.

23 J. A. Zienkiewicz, K. Kałduńska, K. Fedoruk, A. J. Barros dos Santos, M. Stefanski, W. Paraguassu, T. M. Muzioł and M. Ptak, Luminescence and dielectric switchable properties of a 1D (1, 1, 1-Trimethylhydrazinium) $\mathrm{PbI_3}$ hybrid perovskitoid, *Inorg. Chem.*, 2022, **61**, 20886–20895.

24 M. Mączka, M. Ptak, A. Gągor, D. Stefańska and A. Sieradzki, Layered lead iodide of $\mathrm{[methylhydrazinium]_2PbI_4}$ with a reduced band gap: Thermochromic luminescence and switchable dielectric properties triggered by structural phase transitions, *Chem. Mater.*, 2019, **31**, 8563–8575.

25 M. Mączka and M. Ptak, Lattice dynamics and structural phase transitions in two-dimensional ferroelectric methylhydrazinium lead bromide investigated using Raman and IR spectroscopy, *J. Phys. Chem. C*, 2022, **126**, 7991–7998.

26 X. N. Hua, W. Q. Liao, Y. Y. Tang, P. F. Li, P. P. Shi, D. Zhao and R. G. Xiong, A room-temperature hybrid lead iodide perovskite ferroelectric, *J. Am. Chem. Soc.*, 2018, **140**, 12296–12302.

27 W. Guo, H. Xu, Y. Ma, Y. Liu, H. Gao, T. Hu, W. Ren, J. Luo and Z. Sun, Electrically switchable persistent spin texture in a two–dimensional hybrid perovskite ferroelectric, *Angew. Chem., Int. Ed.*, 2023, **62**, 202300028.

28 K. Ding, H. Ye, C. Su, Y. A. Xiong, G. Du, Y. M. You, Z. X. Zhang, S. Dong, Y. Zhang and D. W. Fu, Superior ferroelectricity and nonlinear optical response in a hybrid germanium iodide hexagonal perovskite, *Nat. Commun.*, 2023, **14**, 2863.

29 T. Zhang, K. Xu, J. Li, L. He, D. W. Fu, Q. Ye and R. G. Xiong, Ferroelectric hybrid organic–inorganic perovskites and their structural and functional diversity, *Natl. Sci. Rev.*, 2023, **10**, 240.

30 J. Guo, S. Y. Zhang, C. H. Zeng, Z. G. Zhou, M. Xie, Z.-Y. Du, C.-T. He, W.-X. Zhang and X.-M. Chen, Temperature-tuned variable confined space for modulating dipolar polarization of a disc-shaped ammonium ion, *J. Phys. Chem. Lett.*, 2023, **14**, 8009–8015.

31 M. Mączka, M. Ptak, A. Gągor, D. Stefańska, J. K. ZarÈ©ba and A. Sieradzki, Methylhydrazinium lead bromide: noncentrosymmetric three-dimensional perovskite with exceptionally large framework distortion and green photoluminescence, *Chem. Mater.*, 2020, **32**, 1667–1673.

32 S. García-Martín, A. Morata-Orrantia, M. H. Aguirre and M. Á. Alario-Franco, Giant barrier layer capacitance effects in the lithium ion conducting material $La_{0.67}Li_{0.25}Ti_{0.75}Al_{0.25}O_3$, *Appl. Phys. Lett.*, 2005, **86**, 043110.

33 R. Federicci, S. Holé, A. F. Popa, L. Brohan, B. Baptiste, S. Mercone and B. Leridon, $Rb_2Ti_2O_5$: Superionic conductor with colossal dielectric constant, *Phys. Rev. Mater.*, 2017, **1**, 032001.

34 X. R. Chen, Z. N. He, Y. Qian, W. Wei, Z. F. Tian and X. M. Ren, Spontaneous strain–spin transition coupling molecular crystal with thermal magnetic memory effect, anisotropic high–κ and switchable dielectric permittivity, *Adv. Sci.*, 2025, e01925.

35 S. Chai, J. Xiong, Y. Zheng, R. Shi and J. Xu, Dielectric phase transition of an A_2BX_4-type perovskite with a pentahedral to octahedral transformation, *Dalton Trans.*, 2020, **49**, 2218–2224.

36 J. Di, J. Chang and S. Liu, Recent progress of two–dimensional lead halide perovskite single crystals: crystal growth, physical properties, and device applications, *EcoMat*, 2020, **2**, e12036.

37 D. S. Shao, Y. R. Kong, Q. Ren, Z. F. Tian and X. M. Ren, Alloys of CoI_2 nanoclusters embedded in the PbI_2 lattice exhibiting high-temperature hysteretic paramagnetic transitions and low-temperature diverse magnetic short-range ordering, *ACS Appl. Nano Mater.*, 2024, **7**, 28486–28495.

38 A. J. Torma, W. Li, H. Zhang, Q. Tu, V. V. Klepov, M. C. Brennan, C. L. McCleese, M. D. Krzyaniak, M. R. Wasielewski, C. Katan, J. Even, M. V. Holt, T. A. Grusenmeyer, J. Jiang, R. Pachter, M. G. Kanatzidis, J. C. Blancon and A. D. Mohite, Interstitial nature of Mn^{2+} doping in 2D perovskites, *ACS Nano*, 2021, **15**, 20550–20561.

39 Q. Ba, A. Meena and A. Jana, Solid-state synthesis and optical studies of water-stable Pb^{2+}-doped Mn^{2+} complexes, *Inorg. Chem.*, 2023, **62**, 19025–19032.

40 L. Ma, D. Guo, M. Li, C. Wang, Z. Zhou, X. Zhao, F. Zhang, Z. Ao and Z. Nie, Temperature-dependent thermal decomposition pathway of organic–inorganic halide perovskite materials, *Chem. Mater.*, 2019, **31**, 8515–8522.

41 J. Błażejowski, J. Szychliński and E. Kowalewska, Thermal reactions of lead (iv) chloride complexes in the solid state: Part VI. Thermal properties, thermochemistry and kinetics of the thermal decomposition of alkanaminium hexachloroplumbates, *Thermochim. Acta*, 1986, **108**, 239–263.

42 T. C. Ehlert, A mass spectrometric study of the sublimation of manganese, *J. Inorg. Nucl. Chem.*, 1969, **31**, 2705–2710.

43 M. T. Güllüoğlu, Y. Erdoğdu and Ş. Yurdakul, Molecular structure and vibrational spectra of piperidine and 4-methylpiperidine by density functional theory and ab initio Hartree–Fock calculations, *J. Mol. Struct.*, 2007, **834**, 540–547.

44 G. Mahalakshmi and V. Balachandran, Molecular structure, vibrational spectra (FTIR and FT Raman) and natural bond orbital analysis of 4-Aminomethylpiperidine: DFT study, *Spectrochim. Acta, Part A*, 2014, **131**, 587–598.

45 P. Yadav, D. Gill, S. Khurana, R. S. Lamba, S. Bhattacharya and S. Sapra, Elucidating the Mn^{2+} dopant sites in two-dimensional Na–In halide perovskite, *J. Phys. Chem. C*, 2023, **127**, 3609–3618.

46 M. C. De Siena, D. E. Sommer, S. E. Creutz, S. T. Dunham and D. R. Gamelin, Spinodal decomposition during anion exchange in colloidal Mn^{2+}-doped $CsPbX_3$ (X = Cl, Br) perovskite nanocrystals, *Chem. Mater.*, 2019, **31**, 7711–7722.

47 W. Zhang, S. Pathak, N. Sakai, T. Stergiopoulos, P. K. Nayak, N. K. Noel, A. A. Haghighirad, V. M. Burlakov, D. W. deQuilettes, A. Sadhanala, W. Li, L. Wang, D. S. Ginger, R. H. Friend and H. J. Snaith, Enhanced optoelectronic quality of perovskite thin films with hypophosphorous acid for planar heterojunction solar cells, *Nat. Commun.*, 2015, **6**, 10030.

48 P. Yadav, D. Gill, S. Khurana, R. S. Lamba, S. Bhattacharya and S. Sapra, Elucidating the Mn^{2+} dopant sites in two-dimensional Na–In halide perovskite, *J. Phys. Chem. C*, 2023, **127**, 3609–3618.

49 Y. Luo, K. Liu, L. Yang, W. Feng, L. Zheng, L. Shen, Y. Jin, Z. Fang, P. Song, W. Tian, P. Xu, Y. Li, C. Tian, L. Xie and Z. Wei, Dissolved-Cl_2 triggered redox reaction enables high-

performance perovskite solar cells, *Nat. Commun.*, 2023, **14**, 3738.

50 J. Tu, H. Li, Z. Cai, J. Zhang, X. Hu, J. Huang, C. Xiong, M. Jiang and L. Huang, Phase change-induced tunable dielectric permittivity of poly (vinylidene fluoride)/polyethylene glycol/graphene oxide composites, *Composites, Part B*, 2019, **173**, 106920.

51 S. Li, K. Takahashi, R. K. Huang, C. Chen, K. Kokado, H. Norihisa, A. Tomoyuki, S. Nishihara and T. Nakamura, Multifunctional triggering by solid-phase molecular motion: Relaxor ferroelectricity, modulation of magnetic exchange interactions, and enhancement of negative thermal expansion, *Chem. Mater.*, 2023, **35**, 2421–2428.

52 L. Wei, Y. Liu, T. Yang, H. Rong, X. Zhao, J. Zhang, J. Luo and Z. Sun, Photo–excited switching and enhancement of dielectric properties in two–dimensional double perovskite phase transition thin films, *Chin. J. Chem.*, 2024, **42**, 3122–2128.